

## Tuning the Electronic and Molecular Structures of Catalytic Active Sites with Titania Nanoligands

Elizabeth I. Ross-Medgaarden,<sup>†</sup> Israel E. Wachs,<sup>\*,†</sup> William V. Knowles,<sup>‡</sup>  
Andrew Burrows,<sup>§</sup> Christopher J. Kiely,<sup>§</sup> and Michael S. Wong<sup>†,||</sup>

*Operando Molecular Spectroscopy and Catalysis Laboratory, Department of Chemical Engineering, Lehigh University, Bethlehem, Pennsylvania 18015, Department of Chemical and Biomolecular Engineering, Rice University, Houston, Texas 77005, Departments of Materials Science and Engineering, Lehigh University, Bethlehem, Pennsylvania 18015, and Department of Chemistry, Rice University, Houston, Texas 77005*

Received December 28, 2007; E-mail: iew0@lehigh.edu

**Abstract:** A series of supported 1–60% TiO<sub>2</sub>/SiO<sub>2</sub> catalysts were synthesized and subsequently used to anchor surface VO<sub>x</sub> redox and surface WO<sub>x</sub> acid sites. The supported TiO<sub>x</sub>, VO<sub>x</sub>, and WO<sub>x</sub> phases were physically characterized with TEM, in situ Raman and UV–vis spectroscopy, and chemically probed with in situ CH<sub>3</sub>OH-IR, CH<sub>3</sub>OH-TPSR and steady-state CH<sub>3</sub>OH dehydration. The CH<sub>3</sub>OH chemical probe studies revealed that the surface VO<sub>x</sub> sites are redox in nature and the surface WO<sub>x</sub> sites contain acidic character. The specific catalytic activity of surface redox (VO<sub>4</sub>) and acidic (WO<sub>5</sub>) sites coordinated to the titania nanoligands are extremely sensitive to the degree of electron delocalization of the titania nanoligands. With decreasing titania domain size, <10 nm, acidic activity increases and redox activity decreases due to their inverse electronic requirements. This is the first systematic study to demonstrate the ability of oxide nanoligands to tune the electronic structure and reactivity of surface metal oxide catalytic active sites.

### 1. Introduction

The potential impact of nanotechnology has generated renewed interest in nanoscale catalytic materials in recent years.<sup>1–3</sup> Early systematic studies with supported metal catalysts clearly demonstrated that nanosized metallic catalytic active sites can influence the catalytic performance of some structure-sensitive catalytic reactions.<sup>4</sup> For structure-sensitive reactions, the specific reactivity with decreasing domain size in the 1–10 nm range of the catalytic active sites can either increase (e.g., oxidation of H<sub>2</sub> to H<sub>2</sub>O in excess H<sub>2</sub> over Pt catalysts) or decrease (e.g., synthesis of NH<sub>3</sub> from N<sub>2</sub> and H<sub>2</sub> over Fe catalysts). For structure-insensitive reactions, however, the specific catalytic activity is independent of the domain size of the metallic catalytic active site (e.g., hydrogenation of cyclohexene over Pt). These reactivity trends have been shown to be dependent on the nature of the interactions of the reactant molecules with the specific surface metal atom arrangements of the catalytic active sites.<sup>4,5</sup> For metal oxide catalytic materials, such a systematic examination and fundamental understanding of the influence of the domain size upon catalytic performance

has yet to be established. The surface structure sensitivity of several specific catalytic reactions over metal oxide surfaces, however, is well documented in the literature.<sup>4,6–10</sup> This suggests that the domain size of metal oxide catalysts should also affect the reactivity of structure sensitive reactions. Such a fundamental framework for nanosized metal oxide catalysts is necessary for guiding the design of potentially novel and improved metal oxide catalytic active sites.

The objective of this report is to systematically examine and establish the reactivity trends, as well as their origins for *nanoscale* metal oxide catalytic active site domains for redox and acidic reactions. The metal oxide materials chosen for this investigation consist of well-defined, model-supported metal oxide catalysts. Supported metal oxide catalysts are composed of an amorphous two-dimensional surface metal oxide overlayer on an oxide substrate<sup>11–13</sup> and are extensively employed in the environmental, energy, and petrochemical industries.<sup>14–16</sup> For supported metal oxide catalytic materials involved in redox

<sup>†</sup> Department of Chemical Engineering, Lehigh University.

<sup>‡</sup> Department of Chemical and Biomolecular Engineering, Rice University.

<sup>§</sup> Departments of Materials Science and Engineering, Lehigh University.

<sup>||</sup> Department of Chemistry, Rice University.

- (1) Fernandez-Garcia, M.; Martinez-Arias, A.; Hanson, J. C.; Rodriguez, J. A. *Chem. Rev.* **2004**, *104*, 4063.
- (2) Ogenko, V. M. *Adsorp. Sci. Technol.* **1996**, *14*, 295.
- (3) Abbet, S.; Heiz, U. *Encycl. Nanosci. Nanotechnol.* **2004**, *6*, 161.
- (4) Boudart, M.; Djega-Mariadassou, G.; *Kinetics of Heterogeneous Catalytic Reactions*; Princeton University Press: Lawrenceville, 1984.
- (5) Thomas, J. M., Thomas, W. J.; *Principles and Practice of Heterogeneous Catalysis*; VCH: Weinheim 1997. Somorjai, G. A. *Introduction to Surface Chemistry and Catalysis*; Wiley: New York, 1994.

(6) Badlani, M.; Wachs, I. E. *Catal. Lett.* **2001**, *75*, 137.

(7) Tatibouet, J. M. *Appl. Catal. A: Gen.* **1997**, *148*, 213.

(8) Khodakov, A.; Olthof, B.; Bell, A. T.; Iglesia, E. *J. Catal.* **1999**, *181*, 205.

(9) Macht, J.; Baertsch, C. D.; May-Lozano, M.; Soled, S. L.; Wong, Y.; Iglesia, E. *J. Catal.* **2004**, *227*, 479.

(10) Farneth, W. E.; Ohuchi, F.; Staley, R. H.; Chowdhry, U.; Sleight, A. W. *J. Phys. Chem.* **1985**, *89*, 2493.

(11) Weckhuysen, B. M.; Wachs, I. E. *Handbook Surf. Interfaces Mater.* **2001**, *1*, 613.

(12) Wachs, I. E. *Catal. Today* **1996**, *27*, 437.

(13) Wachs, I. E. *Catalysis (Specialist Periodical Reports)* **1997**, *13*, 37.

(14) Thomas, C. T. *Catalytic Processes and Proven Catalysts*; Academic Press: New York, 1970.

(15) Weissmermel, K.; Arpe, H.-J. *Industrial Organic Chemistry*; Verlag Chemie: Weinheim, 1978.

reactions, the most significant parameter affecting the specific reactivity of the catalytic active site is the specific oxide support ligand (e.g.,  $\text{Al}_2\text{O}_3$ ,  $\text{TiO}_2$ ,  $\text{ZrO}_2$ , etc.). The turnover frequency (TOF), defined as the number of molecules converted per catalytic active site per second, can vary by as much as  $\sim 10^3$  for such catalytic systems when the specific oxide support ligand is varied.<sup>13,17</sup> Consequently, the influence of oxide nanoligand substrates upon the specific reactivity of redox and acidic catalytic active sites of supported metal oxide catalysts is the focus of this communication.

## 2. Experimental Section

**2.1. Catalyst Synthesis. 2.1.1. Preparation of  $\text{TiO}_x/\text{SiO}_2$  Catalysts.** The silica support material, amorphous  $\text{SiO}_2$  (Cabot, Cab-O-Sil fumed silica EH-5, S.A.  $\approx 332 \text{ m}^2/\text{g}$ ), was employed and found to be more easily handled by an initial water pretreatment and calcination at 773 K for 4 h without changing the material properties. The  $\text{TiO}_2/\text{SiO}_2$  supported oxide catalysts were prepared by the incipient-wetness impregnation of isopropanol solutions of titanium isopropoxide ( $\text{Ti}(\text{O}-\text{Pr})_4$ , Alfa Aesar, 99.999%). The silica support was initially dried for 2 h at 393 K to remove the physisorbed water prior to catalyst preparation inside a glovebox (Vacuum Atmospheres, Omni-Laboratory VAC 101965) under a continuously flowing  $\text{N}_2$  (Airgas, Ultra High Purity) environment. After impregnation at room temperature, the samples were kept inside the glovebox to dry overnight under flowing  $\text{N}_2$ . The calcination of the  $\text{TiO}_2/\text{SiO}_2$  samples entailed ramping at 1 K/min to 393 K in flowing  $\text{N}_2$  for 2 h, and then subsequently followed by another 1 K/min ramp under flowing air (Airgas, Zero grade) to 773 K for 4 h. A two-step preparation procedure was employed to prepare samples with loading higher than 8 wt %  $\text{TiO}_2$ . The second impregnation followed the same procedure described above using 8%  $\text{TiO}_2/\text{SiO}_2$  as the starting material to prepare 10%, 12%, and 15%  $\text{TiO}_2/\text{SiO}_2$  catalysts. Multiple impregnation steps were used to prepare samples with loadings higher than 15%  $\text{TiO}_2$ .

**2.1.2. Preparation of  $\text{WO}_x/\text{TiO}_2/\text{SiO}_2$  Catalysts.** Highly dispersed (5 wt %) supported tungsten oxide catalysts were prepared by the incipient-wetness impregnation of aqueous solutions of ammonium metatungstate,  $(\text{NH}_4)_{10}\text{W}_{12}\text{O}_{41} \cdot 5\text{H}_2\text{O}$  (Pfaltz and Bauer, 99.5% purity) on the various  $\text{TiO}_2/\text{SiO}_2$  materials. The samples were dried overnight under ambient conditions and were subsequently dried in flowing air (Airgas, Zero grade) at 393 K for 1 h and calcined in flowing air (Airgas, Zero grade) at 723 K for 4 h.

**2.1.3. Preparation of  $\text{VO}_x/\text{TiO}_2/\text{SiO}_2$  Catalysts.** Highly dispersed (5 wt %) supported vanadium oxide catalysts were prepared by the incipient-wetness impregnation of isopropanol solutions of vanadium triisopropoxide ( $\text{VO}[\text{CHO}(\text{CH}_3)_2]_3$ , Alfa Aesar, 97%) onto the various  $\text{TiO}_2/\text{SiO}_2$  catalysts. The preparation was performed inside a glovebox with continuously flowing  $\text{N}_2$  (Airgas, Ultra High Purity), and the  $\text{TiO}_2/\text{SiO}_2$  support materials were initially dried at 393 K to remove the physisorbed water before impregnation. After impregnation at room temperature, the samples were kept inside the glovebox under flowing  $\text{N}_2$  overnight. The calcination of the  $\text{VO}_x/\text{TiO}_2/\text{SiO}_2$  samples entailed ramping at 1 K/min to 393 K in flowing  $\text{N}_2$  for 2 h, and then subsequently followed by another 1 K/min ramp under flowing air (Airgas, Zero grade) to 773 K for 4 h.

**2.2. Catalyst Characterization. 2.2.1. In Situ Raman Spectroscopy.** Raman spectroscopy was used to obtain the molecular structures of the supported  $\text{TiO}_2/\text{SiO}_2$ ,  $\text{VO}_x/\text{TiO}_2/\text{SiO}_2$ , and  $\text{WO}_x/$

$\text{TiO}_2/\text{SiO}_2$  catalysts with a visible (532 nm) laser excitation on a single stage Horiba–Jobin Yvon Laboratory Ram-HR Raman spectrometer equipped with a confocal microscope (Olympus BX-30) and a notch filter (Kaiser Super Notch). The visible excitation was generated by Nd:YAG doubled diode pumped laser (Coherent Compass 315M-150; output power of 150 mW with sample power 10 mW) with the scattered photons directed into a single monochromator and focused onto a UV-sensitive liquid- $\text{N}_2$  cooled CCD detector (Horiba–Jobin Yvon CCD-3000V) having a spectral resolution of  $\sim 2 \text{ cm}^{-1}$  for the given parameters. The Raman spectrometer was also equipped with an environmentally controlled high-temperature environmental cell (Linkam, TS1500) that examined the catalyst samples in loose powder form ( $\sim 5\text{--}10 \text{ mg}$ ) and also allowed for control of both the temperature and gaseous composition. In situ Raman spectra were collected for the supported tungsten oxide catalysts after dehydration at 723 K for 1 h in flowing 10%  $\text{O}_2/\text{He}$  (Airgas, certified, 9.735%  $\text{O}_2/\text{He}$ , ultrahigh purity and hydrocarbon-free, 30 mL/min) to desorb the adsorbed moisture and the spectra of the dehydrated samples were collected after cooling the catalysts back to 393 K in the flowing 10%  $\text{O}_2/\text{He}$  gas to ensure that the catalyst surface was void of moisture. The spectral acquisition time employed was 20 scans of 20 s/scan for a total of  $\sim 7 \text{ min/spectrum}$ . System alignment was verified daily using a silica reference standard provided by Horiba–Jobin Yvon.

**2.2.2. In Situ  $\text{CH}_3\text{OH}$  Infrared (IR) Spectroscopy.** In situ Fourier transform mid-infrared diffuse reflectance spectroscopy of chemisorbed methanol ( $\text{CH}_3\text{OH}$ -FTIR DRS) on supported  $\text{TiO}_2/\text{SiO}_2$ ,  $\text{VO}_x/\text{TiO}_2/\text{SiO}_2$ , and  $\text{WO}_x/\text{TiO}_2/\text{SiO}_2$  catalysts was performed by a purged single-beam Bio-Rad/Digilab Excalibur FTS4000 spectrometer equipped with KBr beamsplitter and DTGS detector. Undiluted powder samples were loaded into a Harrick Scientific cell (HVC-DRP3) with KBr windows and  $\text{N}_2$ -purged Praying Mantis chamber (DRP-XXX). An auxiliary thermocouple was installed just below the powder surface to measure catalyst temperature. Prior to each sample analysis, the diffuse reflectance accessories were adjusted with an alignment jig to provide  $>40\%$  diffuse reflectance and specular reflectance less than 10% of the diffuse reflectance value at  $2500 \text{ cm}^{-1}$  compared to open beam path transmittance.

The sample procedure was developed from refs 18 and 19 and references within. Powders were heated to 673 K (15 K/min) for 30 min, oxidized in 100 mL/min dry air for 30 min to 673 K, cooled to 423 K in air to minimize thermal reduction<sup>20</sup> (although oxidation states were not experimentally verified), and cooled to 383 K under vacuum. After collecting a baseline spectrum of the pretreated virgin sample at 383 K in vacuum for the Kubelka–Munk reference, each sample was exposed to gas-phase methanol taken from the headspace of room-temperature liquid methanol under vacuum. After reaching surface saturation, the in situ cell was subsequently evacuated to remove weakly bound methoxy species. Next, infrared spectra were collected ever 5 min at a resolution of  $2 \text{ cm}^{-1}$  using 100 signal-averaged scans in the range  $400\text{--}4000 \text{ cm}^{-1}$  until no further spectral changes were observed. Only the final spectra, ratioed to their respective backgrounds, are included in the present report.

The Kubelka–Munk function<sup>21</sup> for infinitely thick samples was used to convert reflectance spectra into equivalent absorption spectra. For each respective catalyst sample, its virgin surface at 383 K after dehydration and oxidation but prior to methanol exposure was used as the reference spectrum.

**2.2.3. In Situ UV–Vis Diffuse Reflectance Spectroscopy (DRS).** The electronic structures of the  $\text{TiO}_x/\text{SiO}_2$  catalysts were obtained with a Varian Cary 5E UV–vis spectrophotometer employing the integration sphere diffuse reflectance attachment (Harrick Praying Mantis Attachment, DRA-2). The finely ground

(16) Farrauto, R. J.; Bartholomew, C. H. *Fundamentals of Industrial Catalytic Processes*; Chapman and Hall: London, 1997.

(17) Wachs, I. E. *Catal. Today* **2005**, *100*, 79.

(18) Boveskov, G. K.; Muzykantov, V. S. *Ann. N.Y. Acad. Sci.* **1973**, *213*, 137.

(19) Davydov, A. A. *Molecular Spectroscopy of Oxide Catalyst Surfaces*; Wiley: Chichester, 2003.

(20) Goulding, M. R.; Thomas, C. B.; Hurditch, R. J. *Solid State Commun.* **1983**, *46*, 451.

(21) Kubelka, P.; Munk, F. Z. *Tech. Phys.* **1931**, *12*, 593.

powder catalyst samples (~20 mg) were loaded into an in situ cell (Harrick, HVC-DR2) and measured in the 200–2200 nm region with a magnesium oxide reflectance standard used as the baseline. The UV–vis spectra of the supported catalysts were obtained after the samples were treated at 673 K for 1 h in flowing 10% O<sub>2</sub>/He (Airgas, certified, 9.735% O<sub>2</sub>/He, ultrahigh purity and hydrocarbon-free, 30 mL/min) to desorb the adsorbed moisture. Below 300 nm, the absorbance signal was unacceptably noisy and a filter (Varian, 1.5ABS) was employed to minimize the background noise. UV–vis DRS studies of the supported MO<sub>x</sub>/TiO<sub>2</sub>/SiO<sub>2</sub> catalysts were not successful in the present work, since absorption from the TiO<sub>2</sub> support exhibits strong absorption in the UV–vis region where VO<sub>x</sub> and WO<sub>x</sub> absorption occurs.

The UV–vis spectra were processed with Microsoft Excel software, consisting of the calculation of the Kubelka–Munk function,  $F(R_{\infty})$  which was extracted from the UV–vis DRS absorbance. The edge energy ( $E_g$ ) for allowed transitions was determined by finding the intercept of the straight line in the low-energy rise of a plot of  $[F(R_{\infty})hv]^{1/n}$ , where  $n = 0.5$  for the direct allowed transition versus  $hv$ , where  $hv$  is the incident photon energy.<sup>21–23</sup>

**2.2.4. High Resolution-Transmission Electron Microscopy (HR-TEM).** Samples for HR-TEM examination were prepared by dispersing the catalyst powder in high-purity ethanol, then allowing a drop of the suspension to evaporate on a lacy carbon film supported by a 300 mesh copper TEM grid. HR-TEM images of the ambient samples were obtained using a JEOL 2200FS transmission electron microscope, having an accelerating voltage of 200 kV, a point-to-point resolution of 0.19 nm, and an information limit of 0.11 nm. Fourier transform (FT) analyses of lattices fringe periodicities and interplanar angles were carried out using digital micrograph. Chemical analysis and EDS mapping were obtained using a VG 603 DSTEM.

**2.3. Reactivity Studies. 2.3.1. Methanol-Temperature Programmed Surface Reaction (TPSR) Spectroscopy.** Methanol-TPSR spectroscopy was performed on an AMI-200 temperature programmed system (Altamira Instruments) linked by a capillary tube to an online quadrupole mass spectrometer (Dycor DyMaxion DME200MS, Ametek Process Instruments). Typically, ~100 mg of catalyst was loaded in a U-type quartz tube and initially pretreated in flowing air at 723 K (Airgas, Ultra Zero grade Air, 30 mL/min) for 40 min to remove any possible adsorbed organic impurities and to dehydrate the sample. To ensure that the surface MO<sub>x</sub> species remained in a fully oxidized state, the pretreated samples were initially cooled to 383 K, where the gas stream was switched to helium (Airgas, Ultra High Purity, 30 mL/min) to flush out any residual gas-phase O<sub>2</sub>. The sample was further cooled to 373 K and held for 30 min to remove any physically adsorbed O<sub>2</sub> and background gases. At 373 K, methanol adsorption was performed by flowing 2000 ppm CH<sub>3</sub>OH/He (Airgas, 30 mL/min) for 30 min, and then the system was purged with flowing helium (Airgas, Ultra High Purity, 30 mL/min) for another 30 min to remove any residual physically adsorbed methanol. Afterward, the sample was heated at a constant heating rate (10 K/min) to 773 K in flowing helium (Airgas, Ultra High Purity, 30 mL/min). The gases exiting from the quartz tube reactor were analyzed with the online mass spectrometer as a function of catalyst temperature. The following  $m/e$  ratios were employed for the identification of the various desorption gases: CH<sub>3</sub>OH,  $m/e = 31$ ; H<sub>2</sub>CO,  $m/e = 30$ ; CH<sub>3</sub>OCH<sub>3</sub>,  $m/e = 45$  and 15 (DME); CO,  $m/e = 28$ ; CO<sub>2</sub>,  $m/e = 44$ ; H<sub>2</sub>O,  $m/e = 18$ ; H<sub>3</sub>COCH,  $m/e = 60$  (MF); and (CH<sub>3</sub>O)<sub>2</sub>CH<sub>2</sub>,  $m/e = 75$  (DMM). For those desorbing molecules that gave rise to several fragments in the mass spectrometer, additional  $m/e$  values were also collected to further confirm their identity. The surface kinetic

parameters ( $E_{\text{act}}$ , and  $k_{\text{rds}}$ ) for the surface methoxy reactions to HCHO and CH<sub>3</sub>OCH<sub>3</sub> are directly obtained from the CH<sub>3</sub>OH-TPSR spectra. The rate-determining step (rds) for the unimolecular surface CH<sub>3</sub>O\* dehydrogenation to HCHO involves breaking the surface methoxy C–H bond.<sup>24</sup> The rds for CH<sub>3</sub>OCH<sub>3</sub> formation involves the unimolecular surface methoxy C–O bond scission.<sup>25</sup> The unimolecular aspect of the rds for the different reaction pathways allows application of the first-order Redhead equation to determine the  $E_{\text{act}}$  for the surface reactions:

$$\frac{E_{\text{act}}}{RT_p^2} = \left(\frac{\nu}{\beta}\right) \exp\left(\frac{-E_{\text{act}}}{RT_p}\right) \quad (1)$$

in which  $T_p$  is the CH<sub>3</sub>OH-TPSR peak temperature of the reaction product,  $R$  is the gas constant (1.987 cal/mol·K),  $\nu = 10^{13} \text{ s}^{-1}$  for first-order kinetics,<sup>24</sup> and  $\beta$  is the heating rate (10 K/min). The rate determining steps,  $k_{\text{rds}}$  (DME) and  $k_{\text{rds}}$  (HCHO), of the surface methoxy intermediate conversion to DME and HCHO, respectively, are a function of  $E_{\text{act}}$  (and hence  $T_p$ ) and determined by

$$k_{\text{rds}} = \nu \exp\left(\frac{-E_{\text{act}}}{RT}\right) \quad (2)$$

in which  $T$  is a reference temperature used for the comparison of  $k_{\text{rds}}$  values, in this case the  $T$  is the temperature at which the steady state methanol dehydrogenation studies are conducted.

**2.3.2. Steady-State Methanol Dehydrogenation to Formaldehyde and Dimethyl Ether.** Steady-state methanol dehydrogenation experiments were conducted in an ambient-pressure reactor consisting of a single-pass downflow fixed bed quartz reactor (0.16 in. ID) packed with finely ground catalyst powder and quartz endcaps. Catalyst loadings (5–30 mg) were chosen to maintain total methanol conversion under 10%, permitting the assumption of differential (i.e., gradientless) reactor conditions. To mimic thermal resistance and estimate catalyst bed temperature, a thermocouple mounted at the same elevation as the catalyst bed was installed inside an identical quartz tube that was fixed to the reactor tube. Both tubes were mounted side-by-side snugly within a 0.5 in. ID metal tube wrapped in heat tape and insulation. Pretreatment consisted of calcining each catalyst at 623 K for 30 min in a 93 mL/min dry flowing gas mixture of Oxygen (Ultra High Purity, Airgas) and Helium (Ultra High Purity, Airgas) controlled at a molar O<sub>2</sub>/He ratio of 14:79 by two independent Coriolis mass flow controllers. The reactor was then cooled to the desired reaction temperature (503 K for VO<sub>x</sub>/TiO<sub>2</sub>/SiO<sub>2</sub> catalysts and 573 K for WO<sub>x</sub>/TiO<sub>2</sub>/SiO<sub>2</sub> catalysts), and the feed gases were bubbled through a liquid methanol saturator (Alfa Aesar, ACS grade). The gas-phase methanol concentration was controlled by the temperature of an overhead condenser, operated at 281 K for these experiments. The final composition of the reactor feed stream was 7%:14%:79% CH<sub>3</sub>OH/O<sub>2</sub>/He at 100 mL/min total flow (ST = 273.15 K, 1 atm). Steady-state performance was determined by averaging 3–4 gas chromatograph (GC) cycles at the reaction temperature and comparing to initial 373 K temperature runs where each catalyst was consistently demonstrated inactive in converting methanol. Blank runs without the catalysts demonstrated negligible methanol conversion in the reactor system. The 0.25 in. OD stainless steel tubing from the reactor outlet to the GC was maintained between 393 and 423 K by heat tape and insulation to minimize condensation of the reactor effluents. The reactor effluent gases were analyzed by an HP5890 Series II online GC (Hewlett-Packard), operated in split mode (308 K for 6 min, ramp 20 K/min to 498 K hold for 5 min), with a 10-port Valco valve diverting two samples in parallel through a CP-sil 5CB capillary column (30 m × 0.32 mm × 5.0 μm, J & W Scientific) to the FID and a 40/60 Carboxene-1000 packed

(22) Gao, X.; Wachs, I. E. *J. Phys. Chem. B* **2000**, *104*, 1261.

(23) Delgass, W. N.; Haller, G. L.; Kellerman, R.; Lunsford, J. H. *Spectroscopy in Heterogeneous Catalysis*; Academic Press: New York, 1979; p 86.

(24) Briand, L. E.; Farneth, W. F.; Wachs, I. E. *J. Catal.* **2002**, *208*, 301.

(25) Kim, T.; Burrows, A.; Kiely, C. J.; Wachs, I. E. *J. Catal.* **2007**, *246*, 370.

(26) Weber, R. S. *J. Catal.* **1995**, *151*, 470.

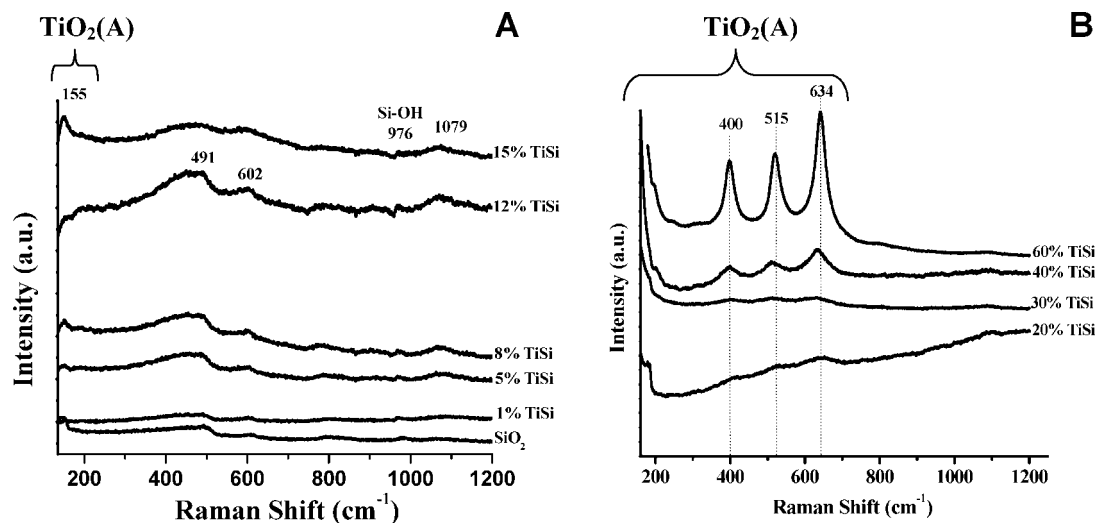


**Figure 1.** Raman spectra (532 nm) under dehydrated conditions as a function of TiO<sub>2</sub> loading of supported TiO<sub>2</sub>/SiO<sub>2</sub> catalysts.

column (5 ft × 1/8 in., Supelco) and to the TCD for determination of the methanol conversion, selectivity, and activity. The steady-state methanol dehydrogenation catalytic data are expressed in terms of TOF, which represents the number of methoxy molecules converted per metal atom per unit time, as illustrated below

$$\text{TOF} = \frac{R_{\text{CH}_3\text{OH}}}{N_s S_{\text{BET}}} \quad (3)$$

where the activity of each catalyst is expressed as the rate of methanol conversion,  $R_{\text{CH}_3\text{OH}}$ ,  $N_s$  represents the surface active site density, and the overall catalyst BET surface area is expressed as  $S_{\text{BET}}$ . Here  $N_s$  is equivalent to the metal oxide surface density assuming 100% exposure of all metal atoms, where surface density is expressed by the following

$$\rho_{\text{surf}} = \frac{\left(\frac{\text{wt \% MO}_x}{100}\right) \left(\frac{1}{M_w \text{ MO}_x}\right) v_{\text{stoich}}}{S_{\text{BET}}} \quad (4)$$

### 3. Results and Discussion

**3.1. Structural Characteristics of Supported MO<sub>x</sub>/TiO<sub>2</sub>/SiO<sub>2</sub> Catalysts.** **3.1.1. Supported TiO<sub>2</sub>/SiO<sub>2</sub> Catalysts.** The Raman spectra of supported TiO<sub>2</sub>/SiO<sub>2</sub> are presented in Figure 1. The XRD amorphous SiO<sub>2</sub> nanoparticles (NPs) possess weak Raman bands at ~400, ~490, ~602, and ~802 cm<sup>-1</sup> originating from vibrations of 2,3,4-membered silica rings, and the band at ~975 cm<sup>-1</sup> is associated with the Si–OH vibration, which decreases slightly with increasing TiO<sub>2</sub> content.<sup>27</sup> Raman bands associated with crystalline TiO<sub>2</sub>(rutile) (142, 445, and 610 cm<sup>-1</sup>), as well as crystalline TiO<sub>2</sub>(brookite) (242, 320, 363, and 407 cm<sup>-1</sup>) are not observed when TiO<sub>2</sub> is supported on the SiO<sub>2</sub> matrix.<sup>27b</sup> However, crystalline bulk TiO<sub>2</sub>(anatase) which gives rise to strong Raman bands at 144, 400, 520, and 643 cm<sup>-1</sup> are observed for samples containing high TiO<sub>2</sub> content (Figure 1). For samples with 12% TiO<sub>2</sub>/SiO<sub>2</sub> or less, crystalline TiO<sub>2</sub>(anatase) NPs are not present since their presence would give rise to strong Raman signals. Instead, the Raman spectrum of the 12% TiO<sub>2</sub>/SiO<sub>2</sub> sample exhibits weak new Raman bands at ~920 and 1080 cm<sup>-1</sup> characteristic of bridging Si–O···Ti

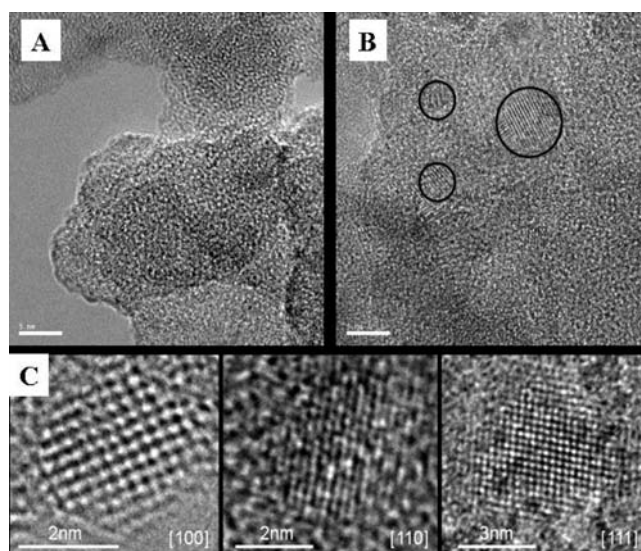


**Figure 2.** Representative HR-TEM images of TiO<sub>2</sub>/SiO<sub>2</sub> containing (A) 12 wt % TiO<sub>2</sub> and (B) 30 wt % TiO<sub>2</sub> with red circles highlighting the crystalline TiO<sub>2</sub>(anatase) NPs, along with (C) a selection HR-TEM images of nanoscale raftlike TiO<sub>2</sub> domains on the SiO<sub>2</sub> support, exhibiting fringe structures that are consistent with [100], [110], and [111] projections of the anatase phase.

**Table 1.** TiO<sub>2</sub> Domain Size for Supported TiO<sub>2</sub>/SiO<sub>2</sub> Catalysts as Determined by HR-TEM

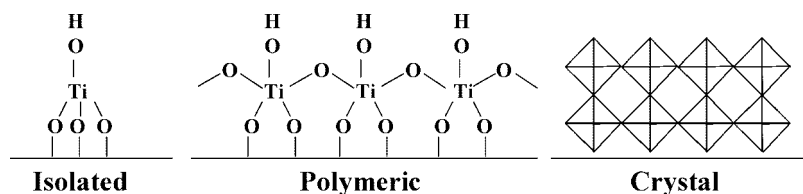
catalyst	structure	domain size (nm)
1% TiO <sub>2</sub> /SiO <sub>2</sub>	isolated surface TiO <sub>4</sub> species	~0.4 <sup>a</sup>
5% TiO <sub>2</sub> /SiO <sub>2</sub>	isolated surface TiO <sub>4</sub> and polymeric surface TiO <sub>5</sub> species	–
12% TiO <sub>2</sub> /SiO <sub>2</sub>	polymeric surface TiO <sub>5</sub> species	~1 <sup>b</sup>
20% TiO <sub>2</sub> /SiO <sub>2</sub>	polymeric surface TiO <sub>5</sub> species and TiO <sub>2</sub> (A)	2–4
30% TiO <sub>2</sub> /SiO <sub>2</sub>	TiO <sub>2</sub> (A)	3–5
40% TiO <sub>2</sub> /SiO <sub>2</sub>	TiO <sub>2</sub> (A)	5–9

<sup>a</sup> Estimated for isolated TiO<sub>4</sub> unit. <sup>b</sup> Estimated for a chain of three surface TiO<sub>5</sub> units.

bonds.<sup>27</sup> The silica surface Si–OH vibration at ~975 cm<sup>-1</sup> is also slightly diminished by anchoring of titania on the SiO<sub>2</sub> substrate.<sup>27</sup> The reaction of titania with the silica surface hydroxyls, formation of the Si–O···Ti bonds and the absence

(27) Gao, X.; Bare, S. R.; Fierro, J. L.; Banaras, M. A.; Wachs, I. E. *J. Phys. Chem. B* **1998**, *102*, 5653. (b) Deo, G.; Turek, A. M.; Wachs, I. E. *Appl. Catal. A: Gen.* **1992**, *91*, 27.

**Scheme 1.** Molecular Structures of Different TiO<sub>2</sub> Domains (A) Isolated Surface TiO<sub>4</sub>, (B) Polymeric Surface TiO<sub>5</sub>, and (C) Crystalline TiO<sub>2</sub>(anatase) Having TiO<sub>6</sub> Octahedral Units



of TiO<sub>2</sub> (anatase) crystallites reflect the presence of a two-dimensional surface TiO<sub>x</sub> layer on the SiO<sub>2</sub> support below 12% TiO<sub>2</sub>/SiO<sub>2</sub>. Thus, the SiO<sub>2</sub>-supported TiO<sub>2</sub>/SiO<sub>2</sub> materials only contain surface TiO<sub>x</sub> species for 12% TiO<sub>2</sub>/SiO<sub>2</sub> and lower loading and TiO<sub>2</sub>(anatase) NPs of varying dimension above 12% TiO<sub>2</sub>/SiO<sub>2</sub> loading. Complementary in situ XANES revealed that the dehydrated 1% TiO<sub>2</sub>/SiO<sub>2</sub> sample consists of isolated surface TiO<sub>4</sub> species on the silica support and that the dehydrated 12% TiO<sub>2</sub>/SiO<sub>2</sub> sample contains polymeric surface TiO<sub>5</sub> species on the silica substrate.<sup>27</sup>

Additional structural information about the SiO<sub>2</sub>-supported titania phase was provided by HR-TEM studies and representative images for the 12% TiO<sub>2</sub>/SiO<sub>2</sub> sample, possessing the polymeric surface titania layer, and the 30% TiO<sub>2</sub>/SiO<sub>2</sub> sample, containing the crystalline titania particles are shown in panels A and B of Figure 2, respectively. The support material primarily consists of ~15 nm amorphous, roughly spherical SiO<sub>2</sub> nanoparticles (NPs) with some minor fraction of the particles being as large as 30 nm. For the 12% TiO<sub>2</sub>/SiO<sub>2</sub> sample (Figure 2A), crystalline TiO<sub>2</sub> particles are not observed, which is consistent with the Raman findings above. Bright field diffraction contrast imaging and selected area electron diffraction patterns also showed no discernible signs of crystalline TiO<sub>2</sub>. However, energy dispersive X-ray spectroscopy (XEDS) on the 12% TiO<sub>2</sub>/SiO<sub>2</sub> sample did confirm the presence of titanium atoms on the support. Crystalline TiO<sub>2</sub> NPs, about 3–5 nm in size, are observable by their characteristic fringe patterns in the 30% TiO<sub>2</sub>/SiO<sub>2</sub> sample (Figure 2B). Interestingly, the TiO<sub>2</sub> NPs form with a raftlike morphology on the silica support, as evidenced by the fact they were never seen in profile. FT analysis of those patches that exhibited crossed lattice fringes was carried out in order to measure the lattice spacing and interplanar angles of these crystalline domains. In the majority of cases, the fringe patterns could be matched to the anatase phase of TiO<sub>2</sub>. A few typical examples of such patches, consistent with the [100], [110], and [111] projections of anatase are shown in Figure 2C. The formation of the TiO<sub>2</sub> (anatase) NPs in the 30% TiO<sub>2</sub>/SiO<sub>2</sub> sample was found to consume the surface TiO<sub>x</sub> species since no discernible titanium signal could be detected by XEDS from the SiO<sub>2</sub> support regions between the TiO<sub>2</sub> NPs. The transformation occurs because of the greater affinity of the surface TiO<sub>x</sub> species for the TiO<sub>2</sub> (anatase) NPs over the relatively inert SiO<sub>2</sub> surface. The titania domain size of the different supported TiO<sub>2</sub>/SiO<sub>2</sub> samples is listed in Table 1, and the molecular structures are shown illustratively in Scheme 1. Such novel raft structures possess properties unlike the typical 3D TiO<sub>2</sub> (anatase) NPs (see below).

The corresponding electronic structures of the series of supported TiO<sub>2</sub>/SiO<sub>2</sub> samples possessing variable titania nanodomain size were examined with in situ UV–vis spectroscopy. UV–vis DRS exclusively provides information about the local electron density of the supported titania phase because of the

weak absorbance by the SiO<sub>2</sub> support.<sup>28</sup> The electron density of nanostructured metal oxide clusters is known to be dependent on the metal oxide domain size, with the local electron density increasing for smaller dimensions and the electrons becoming more delocalized for larger dimensions.<sup>26</sup> The edge energy,  $E_g$  (eV), values for the different supported titania materials increase continuously as the TiO<sub>x</sub> domain size decreases as shown in Figure 3. Larger edge energy values correspond to higher local electron density and less electron delocalization, which also generally corresponds to a less reducible metal oxide. This trend reflects the well-known quantum confinement effect for small dimensions.<sup>29</sup>

In summary, the chosen synthesis method successfully varied the SiO<sub>2</sub>-supported titania domain size over a wide range, in the critical sub-10 nm domain size, that would allow for examination of the oxide nanoligand substrate domain size upon the structure and reactivity of different types of supported catalytic active sites. It is, thus, anticipated that redox reactions that require electrons should be favored by large domain size and acidic reactions that do not require electrons should be favored by small domain size.<sup>4,30,31</sup>

**3.1.2. Supported WO<sub>3</sub>/TiO<sub>2</sub>/SiO<sub>2</sub> Catalysts.** The molecular nature of the deposited tungsten oxide phase on the TiO<sub>2</sub>/SiO<sub>2</sub> support was determined with in situ Raman spectroscopy, and the spectra are presented in Figure 4. The Raman spectra reveal that crystalline WO<sub>3</sub> NPs are not present (absence of strong bands at 804, 710, and 270 cm<sup>-1</sup>) and, consequently, that the active tungsten oxide is 100% dispersed as surface WO<sub>x</sub> species on the TiO<sub>2</sub>/SiO<sub>2</sub> support (Raman bands in the ~1000 cm<sup>-1</sup> range).<sup>12</sup> The broad Raman band at ~1080 cm<sup>-1</sup> is associated with the bridging Ti–O–Si vibration and is not related to the surface WO<sub>x</sub> vibrations. For dehydrated WO<sub>3</sub>/SiO<sub>2</sub>, the primary Raman W=O vibration occurs at ~980 cm<sup>-1</sup>, characteristic of dioxo (O=W=O) WO<sub>4</sub> species,<sup>32</sup> with a weaker vibration at ~1010 cm<sup>-1</sup>, associated with monoxo (W=O) WO<sub>5</sub> species.<sup>12,32–36</sup> The Raman spectra for all of the dehydrated supported WO<sub>x</sub>/TiO<sub>2</sub>/SiO<sub>2</sub> catalysts, however, are dominated by the monoxo W=O vibration at ~1010 cm<sup>-1</sup>. The constant vibration of the W=O bond with titania content indicates that the molecular structure of the surface WO<sub>x</sub> species is the same for all supported TiO<sub>2</sub>/SiO<sub>2</sub> catalysts. The position of this Raman band also reveals that the surface WO<sub>x</sub> species preferentially coordinate to TiO<sub>x</sub> sites rather than SiO<sub>2</sub> sites and the titania nanoligand

(28) Gao, X.; Wachs, I. E. *J. Phys. Chem. B* **2000**, *104*, 1261.

(29) Fernandez-Garcia, M. *Catal. Rev.* **2002**, *44*, 1.

(30) Liu, H.; Cheung, P.; Iglesia, E. *J. Catal.* **2003**, *217*, 222.

(31) Chen, M. S.; Goodman, D. W. *Science* **2004**, *306*, 252.

(32) Lee, E.; Wachs, I. E. *J. Phys. Chem. C* **2007**, *111*, 14410–14425.

(33) Kim, D. S.; Ostromecki, M.; Wachs, I. E. *J. Mol. Catal. A Chem.* **1996**, *106*, 93.

(34) Vuurman, M. A.; Wachs, I. E. *J. Phys. Chem.* **1992**, *96*, 5008.

(35) Jarupatrakorn, J.; Coles, M. P.; Tilley, T. D. *Chem. Mater.* **2005**, *17*, 818.

(36) Nakamoto, K. *Infrared and Raman Spectra of Inorganic Coordination Compounds*, 5th ed.; Wiley and Sons: New York, 1997.

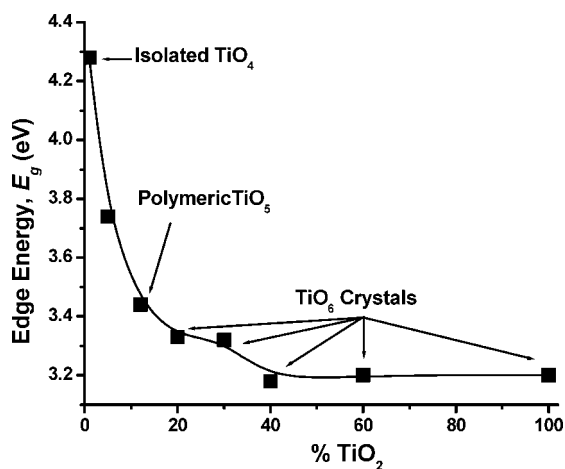


**Figure 3.** UV-vis edge energy,  $E_g$  (eV), as a function of %  $\text{TiO}_2$  loading for supported  $\text{TiO}_2/\text{SiO}_2$  catalysts.

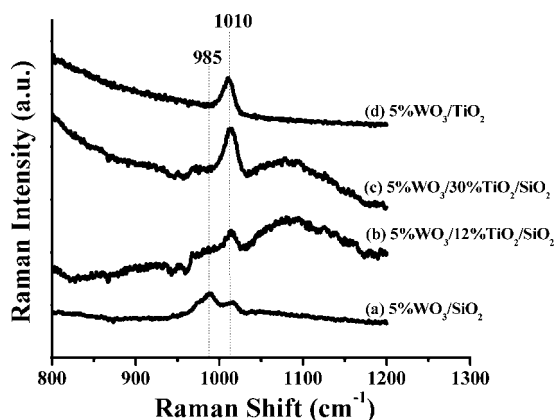


**Figure 4.** Raman Spectra (532 nm) under dehydrated conditions for (A) 5%  $\text{WO}_3/\text{SiO}_2$ , (B) 5%  $\text{WO}_3/12\% \text{TiO}_2/\text{SiO}_2$ , (C) 5%  $\text{WO}_3/30\% \text{TiO}_2/\text{SiO}_2$ , and (D) 5%  $\text{WO}_3/\text{TiO}_2$ .

alters the surface  $\text{WO}_x$  molecular structure. This preferential binding of surface  $\text{WO}_x$  to the  $\text{TiO}_x$  nanoligand over the  $\text{SiO}_2$  support sites was further confirmed by methanol IR chemisorption studies that discriminated between surface  $\text{Si}-\text{OCH}_3$ ,  $\text{Ti}-\text{OCH}_3$ , and  $\text{W}-\text{OCH}_3$  vibrations and are presented in Figure 5. The  $\text{CH}_3\text{OH}$ -IR spectra demonstrate that the  $\text{Ti}-\text{OCH}_3$  IR bands ( $2920$  and  $2822 \text{ cm}^{-1}$ ) are significantly diminished relative to the  $\text{Si}-\text{OCH}_3$  IR bands in the presence of surface  $\text{W}-\text{OCH}_3$  species because the surface  $\text{WO}_x$  sites are preferentially coordinated to the surface titania nanoligands. Note that the  $\text{Ti}-\text{OCH}_3$  IR vibrations are almost absent for the 5%  $\text{WO}_3/x\% \text{TiO}_2/\text{SiO}_2$  catalysts and that  $\sim 5\% \text{WO}_x$  covers  $\sim 5\% \text{TiO}_2$ . The preferential anchoring of  $\text{WO}_x$  on  $\text{TiO}_x$  is related to the higher surface free energy of titania relative to silica, and the facile surface diffusion of surface  $\text{WO}_x$  at modest temperatures. The thermodynamic driving force is lowering of the system surface free energy (replacing higher free energy surface  $\text{Ti}-\text{OH}$  bonds with lower surface free energy terminal  $\text{W}=\text{O}$  bonds) and the kinetics are facilitated by surface diffusion of the metal oxides (related to the modest  $\text{WO}_3$  Tammann temperature<sup>35,37</sup>). Thus, both location and structure of surface  $\text{WO}_x$  species are controlled

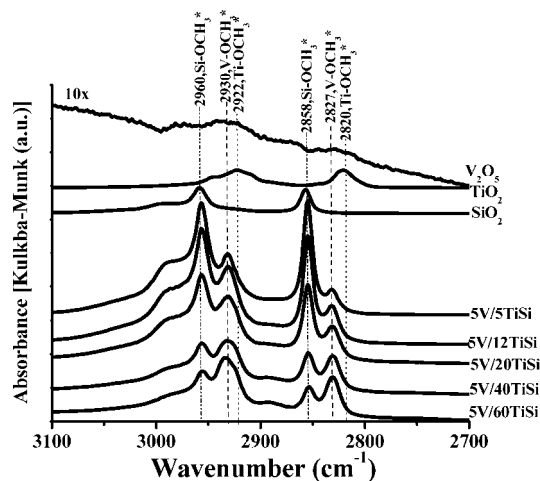


**Figure 5.** Infrared spectra of adsorbed methoxylated surface species in the C-H stretching region for 5%  $\text{WO}_3/x\% \text{TiO}_2/\text{SiO}_2$  catalysts.

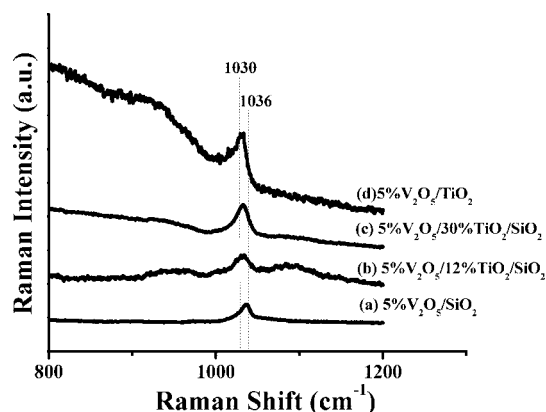


**Figure 6.** Raman spectra (532 nm) under dehydrated conditions for (A) 5%  $\text{V}_2\text{O}_5/\text{SiO}_2$ , (B) 5%  $\text{V}_2\text{O}_5/12\% \text{TiO}_2/\text{SiO}_2$ , (C) 5%  $\text{V}_2\text{O}_5/30\% \text{TiO}_2/\text{SiO}_2$ , and (D) 5%  $\text{V}_2\text{O}_5/\text{TiO}_2$ .

by the titania nanoligands and the surface  $\text{WO}_x$  structure is independent of titania loading.

**3.1.3. Supported  $\text{VO}_x/\text{TiO}_2/\text{SiO}_2$  Catalysts.** The nature of the dehydrated supported vanadia phase on the  $\text{TiO}_2/\text{SiO}_2$  support was determined with in situ Raman spectroscopy and the spectra are shown in Figure 6. The Raman spectra reveal that crystalline  $\text{V}_2\text{O}_5$  NPs are not present (absence of strong band at  $994 \text{ cm}^{-1}$ ) and that the surface  $\text{VO}_x$  species is 100% dispersed on the  $\text{TiO}_2/\text{SiO}_2$  support (Raman band  $\sim 1036 \text{ cm}^{-1}$ ).<sup>39</sup> Previous XANES and solid-state  $^{51}\text{V}$  NMR characterization revealed that the dehydrated surface  $\text{VO}_x$  species always possessed  $\text{VO}_4$  coordination.<sup>39-42</sup> For the dehydrated supported  $\text{V}_2\text{O}_5/\text{SiO}_2$  catalyst, the Raman band of the monoxo surface  $\text{VO}_4$  species vibrates at  $\sim 1036-1040 \text{ cm}^{-1}$ .<sup>39</sup> For the dehydrated supported  $\text{V}_2\text{O}_5/\text{TiO}_2$  catalyst, the monoxo surface  $\text{VO}_4$  species band appears at  $\sim 1027-1031 \text{ cm}^{-1}$ .<sup>42</sup> The surface  $\text{VO}_4$  species, unlike the surface  $\text{WO}_x$  species, always possess the monoxo  $\text{V}=\text{O}$  structure and do not change coordination with different support ligands.<sup>40,41</sup> Nevertheless, there is a slight shift in the terminal  $\text{V}=\text{O}$  bond

(37) Knözinger, H.; Taglauer, E. Spreading and Wetting. In *Preparation of Solid Catalysts*; Ertl, G., Knözinger, H., Weitkamp, J., Eds.; Wiley-VCH: Weinheim, 1999.

(38) Knozinger, H.; Taugler, E. *Catalysis (Specialist Periodical Reports)* **1993**, 10, 1.

(39) Gao, X.; Bare, S. R.; Weckhuysen, B. M.; Wachs, I. E. *J. Phys. Chem. B* **1998**, 102, 10842.

(40) Eckert, H.; Wachs, I. E. *J. Phys. Chem.* **1989**, 93, 6796.

(41) Das, N.; Eckert, H.; Hu, H.; Wachs, I. E.; Walzer, J. F.; Feher, F. J. *Phys. Chem.* **1993**, 97, 8240.

(42) Gao, X.; Bare, S. R.; Wachs, I. E. *J. Phys. Chem. B* **1999**, 103, 618.

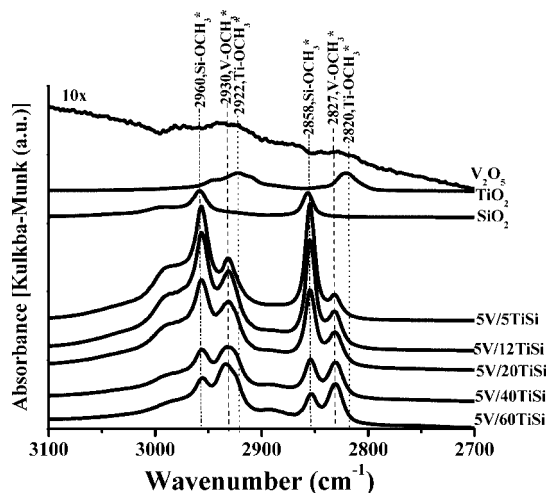
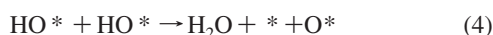
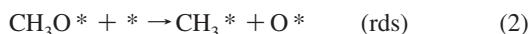


**Figure 7.** Infrared spectra of adsorbed methoxylated surface species in the C–H stretching region for 5%  $\text{VO}_x/x\% \text{TiO}_2/\text{SiO}_2$  catalysts.

when it is coordinated to different oxide support ligands.<sup>43</sup> The Raman band of the terminal  $\text{V}=\text{O}$  bond at  $\sim 1032 \text{ cm}^{-1}$  reflects the preferential coordination of the surface  $\text{VO}_4$  species to the supported titania phase over the silica support. This is further confirmed by  $\text{CH}_3\text{OH}$ -IR spectra that demonstrate the preferential anchoring of the surface  $\text{VO}_4$  species on the titania sites (see Figure 7), since  $\text{Ti}-\text{OCH}_3$  IR vibrations ( $2922$  and  $2820 \text{ cm}^{-1}$ ) are almost absent from the 5%  $\text{V}_2\text{O}_5/x\% \text{TiO}_2/\text{SiO}_2$  catalysts reflecting that the Ti sites are preferentially being covered by the surface  $\text{VO}_x$  species. In situ X-ray absorption near edge spectroscopy (XANES) results are also consistent with the preferential coordination of the surface  $\text{VO}_4$  species to the titania nanoligands since the polymeric surface  $\text{TiO}_5$  species increase their coordination to  $\text{TiO}_6$  with anchoring of the surface vanadia.<sup>42</sup> Furthermore, the relatively constant Raman band at  $\sim 1032 \text{ cm}^{-1}$  indicates that the same surface  $\text{VO}_x$  species are present for all the  $\text{TiO}_2/\text{SiO}_2$  samples. Thus, similar to the supported  $\text{WO}_x/\text{TiO}_2/\text{SiO}_2$  catalyst system, the catalytic active surface  $\text{VO}_4$  species preferentially anchor or self-assemble at the surface titania sites.

**3.2. Catalytic Properties of Supported  $\text{MO}_x/\text{TiO}_2/\text{SiO}_2$  Catalysts.** **3.2.1. Supported  $\text{WO}_x/\text{TiO}_2/\text{SiO}_2$  Catalysts.** The surface catalytic chemistry of the new monoxo surface  $\text{WO}_5$  species bonded to the titania nanoligands catalysts was chemically probed with  $\text{CH}_3\text{OH}$  dehydration to  $\text{CH}_3\text{OCH}_3$  and  $\text{H}_2\text{O}$ , which only takes place over surface acidic catalytic active sites.<sup>6,7</sup> Unlike the redox character of the dioxo surface  $\text{WO}_4$  species on  $\text{SiO}_2$  that yield  $\text{H}_2\text{CO}$ , the monoxo surface  $\text{WO}_5$  species on  $\text{TiO}_2/\text{SiO}_2$  behave as acidic sites since they exclusively yield DME as the reaction product. Methanol dehydration to dimethyl ether proceeds via the following elementary reaction steps:



with the breaking of the C–O bond representing the first-order rds. The asterisk represents an empty or uncoordinated W site, whereas  $\text{X}^*$  represents an occupied surface W site ( $\text{X} = \text{O}^*$ ,

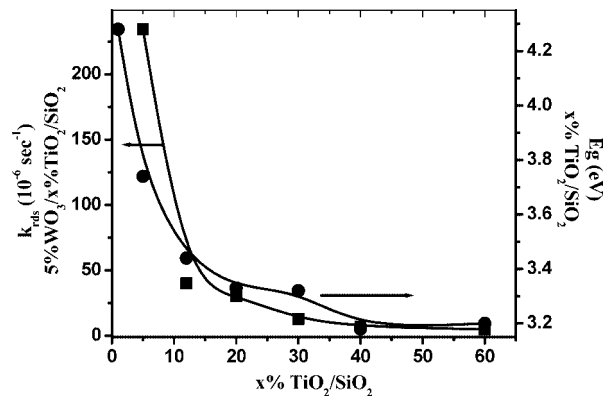


**Figure 8.** First-order rate constant for C–O bond breaking of the surface  $\text{CH}_3\text{O}^*$  intermediate in formation of  $\text{CH}_3\text{OCH}_3$  and titania nanoligand  $E_g$  as a function of titania loading for the supported 5%  $\text{WO}_3/x\% \text{TiO}_2/\text{SiO}_2$  catalyst system.

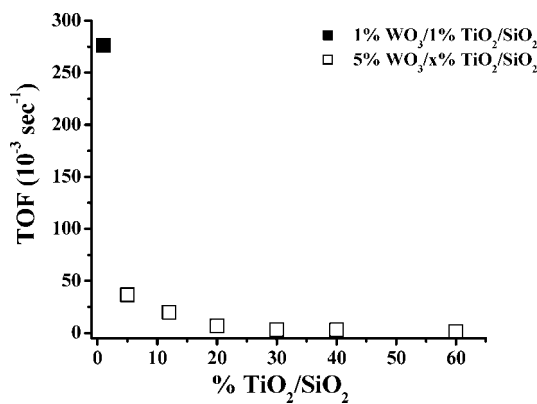
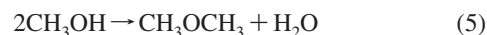


**Figure 9.** Catalytic acidity, TOF, for  $\text{CH}_3\text{OH}$  dehydration to DME over 5%  $\text{WO}_3/x\% \text{TiO}_2/\text{SiO}_2$  catalysts as a function of  $\text{TiO}_2$  loading for a steady-state reaction temperature of 573 K.

$\text{HO}^*$ ,  $\text{CH}_3^*$ , or  $\text{CH}_3\text{O}^*$ ).<sup>4</sup> The overall reaction stoichiometry is given by



and shows that oxygen from the catalytic active surface  $\text{WO}_5$  sites is not consumed in this surface acidic reaction. The  $\text{CH}_3\text{OH}$  dehydration reaction over the supported  $\text{WO}_3/\text{TiO}_2/\text{SiO}_2$  catalysts was found to be 100% selective toward  $\text{CH}_3\text{OCH}_3$  formation. This reflects the catalytic dominance of the acidic surface  $\text{WO}_x$  sites in these catalysts. The first-order reaction rate constants for scission of the C–O bond on the supported  $\text{WO}_3/\text{TiO}_2/\text{SiO}_2$  catalysts were determined with  $\text{CH}_3\text{OH}$ -TPSR spectroscopy<sup>44</sup> and are compared with the corresponding titania  $E_g$  values as a function of the catalyst titania content in Figure 8. The monotonic increase in  $k_{\text{rds}}$  with decreasing domain size follows almost the exact same trend as the  $E_g$  values of the titania nanoligands as a function of titania domain size. Similar trends were also obtained for steady-state  $\text{CH}_3\text{OH}$  dehydration over the supported  $\text{WO}_3/\text{TiO}_2/\text{SiO}_2$  catalysts as a function of the titania nanoligand domain size (Figure 9). These findings reveal that higher  $E_g$  values of the titania nanoligand, with less electron delocalization, correspond to enhanced acidic activity of the surface  $\text{WO}_5$  catalytic active sites. Thus, small  $\text{TiO}_2$  domains decrease the extent of electron delocalization and enhance the catalytic activity of nonreducible catalytic acid sites. *This is direct evidence for the influence of nanostructured oxide*

(43) Deo, G.; Wachs, I. E. *J. Catal.* **1994**, *146*, 335.

(44) Wang, X.; Wachs, I. E. *Catal. Today* **2004**, *96*, 211.

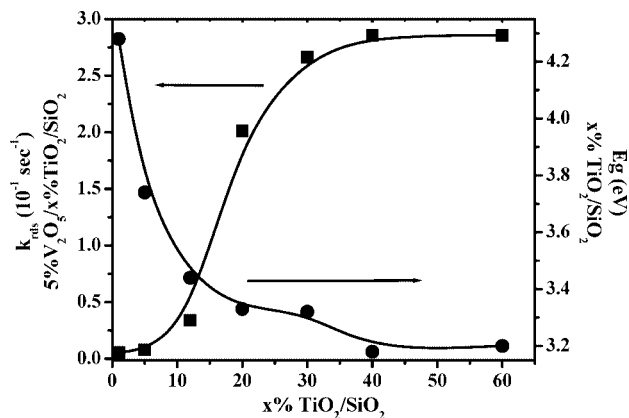
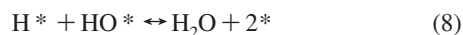
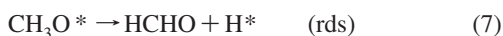


**Figure 10.** First-order rate constant for C–H bond breaking of the surface  $\text{CH}_3\text{O}^*$  intermediate in formation of HCHO and titania nanoligand  $E_g$  as a function of titania loading for the supported 5%  $\text{V}_2\text{O}_5/x\%$   $\text{TiO}_2/\text{SiO}_2$  catalyst system.

support dimension and  $E_g$  on catalytic activity of surface acidic sites.<sup>25</sup>

**3.2.2. Supported  $\text{VO}_x/\text{TiO}_2/\text{SiO}_2$  Catalysts.** The surface catalytic chemistry of the surface  $\text{VO}_4$  species on the titania nanoligands was chemically probed with  $\text{CH}_3\text{OH}$  oxidation to HCHO and  $\text{H}_2\text{O}$ , which only takes place on surface redox catalytic active sites.<sup>6,7,45</sup> Formation of  $\text{CH}_3\text{OCH}_3$  was not observed, which reflects the dominance of the redox nature of the surface  $\text{VO}_4$  species. Methanol oxidation to formaldehyde proceeds via the following elementary reaction steps:



with the breaking of the C–H bond of the surface  $\text{CH}_3\text{O}^*$  intermediate representing the first-order rds. The overall reaction stoichiometry is given by eq 9, which shows that oxygen from the catalytic active surface  $\text{VO}_4$  species is consumed in this surface redox reaction.



The consumption of one oxygen atom is accompanied by the reduction of the surface vanadia species by two electrons:



The first-order reaction rate constants for breaking of the C–H bond of the surface  $\text{CH}_3\text{O}^*$  intermediates were determined with  $\text{CH}_3\text{OH}$ -TPSR<sup>44,45</sup> and are compared with the  $E_g$  values of the titania nanoligands as a function of the titania content in the catalysts, as shown in Figure 10. The monotonic decrease in  $k_{\text{rds}}$  with decreasing titania domain size varies inversely to the increasing  $E_g$  value of the titania nanoligands. Similar trends were also obtained for steady-state methanol oxidative dehydrogenation over the supported  $\text{VO}_x/\text{TiO}_2/\text{SiO}_2$  catalysts as a

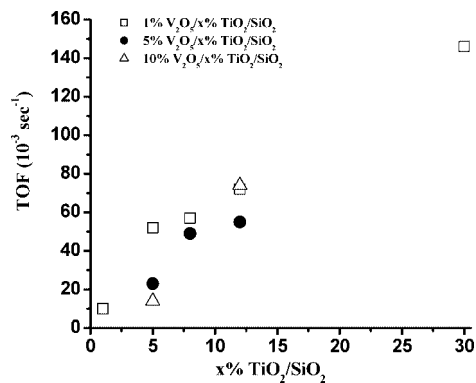


**Figure 11.** Catalytic activity, TOF, for  $\text{CH}_3\text{OH}$  oxidative dehydrogenation to HCHO over 5%  $\text{VO}_x/x\%$   $\text{TiO}_2/\text{SiO}_2$  catalysts as a function of  $\text{TiO}_2$  loading for a steady-state reaction temperature of 503 K.

function of the titania nanoligand domain size (Figure 11). These findings reveal that lower  $E_g$  values, with greater electron delocalization, correspond to enhanced redox activity of surface  $\text{VO}_4$  catalytic active sites. Thus, large  $\text{TiO}_2$  domains increase the extent of electron delocalization and enhance the catalytic activity of the reducible catalytic redox sites.

#### 4. Conclusions

Titania nanoligands, in the sub-10 nm range, with variable electronic structures were successfully synthesized on a relatively inert  $\text{SiO}_2$  support. The catalytic active surface redox ( $\text{VO}_x$ ) and acidic ( $\text{WO}_x$ ) sites were found to preferentially self-assemble at the titania nanoligands in the mixed  $\text{TiO}_2/\text{SiO}_2$  support materials. For surface redox sites, increasing the domain size of the titania nanoligands significantly enhances the specific catalytic activity by delocalization of the titania electrons. For the surface acidic sites, in contrast, decreasing the titania domain size significantly enhances the catalytic activity by localization of the titania electrons. The inverse responses of surface redox and surface acidic sites to the electron density of the titania nanoligands reflect the different reactivity requirements of surface redox and surface acidic metal oxide catalytic active sites. This is the first direct evidence for the influence of nanostructured oxide support dimension and optical  $E_g$  values on the catalytic activity of surface  $\text{MO}_x$  sites. In spite of the incomplete control of the  $\text{TiO}_2$  domain size, which is intrinsic to the conventional catalyst impregnation route employed, these experimental findings clearly demonstrate that the catalytic active monoxo surface  $\text{WO}_5$  and  $\text{VO}_4$  species coordinate to the  $\text{TiO}_2$  domains on  $\text{SiO}_2$ . Thus, varying the local electron density of oxide nanoligand supports allows for the tuning of the specific activity characteristics of surface metal oxide catalytic active sites as shown for the supported  $\text{VO}_x/\text{TiO}_2/\text{SiO}_2$  and  $\text{WO}_x/\text{TiO}_2/\text{SiO}_2$  catalyst systems.

**Acknowledgment.** The authors gratefully acknowledge the financial support by the NSF NIRT Grant No. 0609018. M.S.W. also acknowledges 3M (NFT Award) for financial support.

JA711456C

(45) Kim, T.; Wachs, I. E. *J. Catal.* **2008**, *255*, 197.